

Importance of surface oxygen vacancies for ultrafast hot carrier relaxation and transport in Cu₂O

Chiara Ricca,^{1,2} Lisa Grad,³ Matthias Hengsberger,³ Jürg Osterwalder,³ and Ulrich Aschauer^{1,2,*}

¹*Department of Chemistry and Biochemistry, University of Bern, Freiestrasse 3, CH-3012 Bern, Switzerland*

²*National Centre for Computational Design and Discovery of Novel Materials (MARVEL), Switzerland*

³*Department of Physics, University of Zurich, Winterthurerstrasse 190, CH-8057 Zurich, Switzerland*

(Dated: March 9, 2021)

Cu₂O has appealing properties as an electrode for photo-electrochemical water splitting, yet its practical performance is severely limited by inefficient charge extraction at the interface. Using hybrid DFT calculations, we investigate carrier capture processes by oxygen vacancies (V_O) in the experimentally observed ($\sqrt{3} \times \sqrt{3}$)R30° reconstruction of the dominant (111) surface. Our results show that these V_O are doubly ionized and that associated defect states strongly suppress electron transport. In particular, the excited electronic state of a singly charged V_O plays a crucial role in the non-radiative electron capture process with a capture coefficient of about 10⁻⁹ cm³/s and a lifetime of 0.04 ps, explaining the experimentally observed ultrafast carrier relaxation. These results highlight that engineering the surface V_O chemistry will be a crucial step in optimizing Cu₂O for photoelectrode applications.

I. INTRODUCTION

Cuprous oxide (Cu₂O) is a promising material for a variety of industrial applications due to its small direct band gap, its high absorbance, the abundance and non-toxicity of its constituent elements and the large flexibility and low cost of Cu₂O-based thin-film preparation methods¹. In particular, cuprous oxide has recently attracted much attention as an electrode material for photo-electrochemical water splitting with efficient light absorption, high positive onset voltage, and high photocurrent density^{2,3}. However, the electrode performance is highly sensitive to the presence of defect states generally appearing within the semiconductor band gap^{4,5}. Such defect states may trap excited charge carriers resulting in a reduction of the generated photovoltage and photocurrent.

In bulk Cu₂O both copper and oxygen vacancies occur, copper vacancies being more abundant and generally leading to *p*-type doping. The (111) facet is the experimentally most studied Cu₂O surface and two ordered surface structures were identified. The first corresponds to the ideal O-terminated and stoichiometric surface with (1 × 1) periodicity. The second is a reconstructed ($\sqrt{3} \times \sqrt{3}$)R30° surface with only 2/3 of the O ions in the outermost surface layer⁶⁻⁸. The exact termination, stoichiometry and atomic structure of the reconstructed surface have been studied by experiment⁶⁻⁸ and theory⁹⁻¹³, associating it most likely with a 1/3 monolayer of ordered oxygen vacancies (V_O)⁶⁻⁸.

Recently, it was suggested that these surface V_O dominantly affect the photocatalytic performance in Cu₂O-based materials under oxygen poor conditions⁵. Comparing electron dynamics at stoichiometric and oxygen deficient Cu₂O-(111) surfaces observed via time-resolved two-photon photoemission (2PPE) indicates that surface rather than bulk defects limit the photovoltage. Excited electrons can drift within the conduction band to the

stoichiometric Cu₂O-(111) surface where they create an energetic electron population that decays with a characteristic time of 10 picoseconds. On the oxygen deficient ($\sqrt{3} \times \sqrt{3}$)R30°-(111) surface, however, no indication of electrons occupying the conduction band was found, but instead electrons are trapped, within 1 picosecond, by low-lying defect states with no further noticeable change of the electron population over a timescale of hundreds of picoseconds. This indicates that V_O associated with the reconstruction likely trap carriers.

Unfortunately, previous experimental^{6-8,14} and theoretical¹⁵⁻¹⁹ work reports contradictory results for V_O in Cu₂O, especially in terms of the thermodynamic stability of different charge states, the position of the corresponding defect levels in the band gap, and consequently their ability to act as efficient carrier traps (see supporting information (SI) Section S3). In addition, these theoretical studies are restricted to the bulk and the experimentally relevant carrier capture at surface defects has never been computationally studied.

Here we investigate the stability and electronic properties of V_O, and the electron and hole trapping processes by these defects at the Cu₂O surface by combining density functional theory (DFT) calculations and photoemission experiments. Accurately computing the electronic properties of Cu₂O is a challenging task, due to the peculiar properties of this oxide: a mainly ionic semiconductor with closed shell Cu⁺ ions and a higher coordination of O than Cu atoms, which leads to large cohesive energies. Semi-local DFT fails to predict the semiconducting character^{1,17}, DFT+*U* approaches also failing to open the band gap due to the fully occupied Cu-3*d*¹⁰ states. All our calculations have hence been performed using hybrid functionals, which can successfully reproduce the band structure of Cu₂O^{18,20}, but are rather expensive for applications in solid-state chemistry, especially with planewave-based codes and for surface/defect calculations that require large supercells. By comparing computed defect levels and electron capture coeffi-

cients with experimental results, we reach a deep understanding of the carrier dynamics and factors limiting photoelectrode performance. In particular, our results demonstrate that the defect states associated with the reconstructed Cu_2O -(111) surface are due to an ordered arrangement of doubly ionized V_O , which effectively trap electrons and strongly suppress electron transport. This indicates that engineering the surface defect chemistry of Cu_2O -based photoelectrodes is crucial to enhance their performance.

II. RESULTS AND DISCUSSION

A. $(\sqrt{3} \times \sqrt{3})\text{R}30^\circ$ - (111) Cu_2O surface

Figure 1 illustrates the slab model used to simulate the unreconstructed (1×1) and reconstructed $(\sqrt{3} \times \sqrt{3})\text{R}30^\circ$ -(111) Cu_2O surfaces within the $(\sqrt{3} \times \sqrt{3})\text{R}30^\circ$ supercell, where the c -axis is perpendicular to the surface plane. The unreconstructed surface consists of O-Cu-O trilayers, with each Cu layer sandwiched between two O layers. The topmost trilayer in the unreconstructed supercell contains four types of atoms: 3 coordinatively unsaturated O atoms (O_{CUS}) in the first layer, 3 coordinatively unsaturated (Cu_{CUS}) and 9 coordinatively saturated Cu atoms (Cu_{CSA}) in the second, and 3 coordinatively saturated O atoms (O_{CSA}) in the third layer. Experiment suggests that the reconstructed oxygen-deficient surface, which we focus on in this work, is associated with a $\frac{1}{3}$ monolayer of charged surface $\text{V}_{\text{O}_{\text{CUS}}}$ forming ordered structures due to mutual electrostatic repulsion⁶⁻⁸.

Surface energies computed for the ideal stoichiometric (0.831 J/m^2) and defective ($0.919/0.931 \text{ J/m}^2$ under O-poor/rich conditions) surface are slightly higher (by about 0.2 J/m^2 and 0.1 J/m^2 respectively) compared to previous semi-local DFT or DFT+ U results¹⁰. The qualitative picture is, however, in agreement, indicating the ideal surface to be slightly more stable than the reconstructed surface, regardless of the O chemical potential. This is also in line with the experimental conditions required to obtain the two surface structures: the ideal surface is generally obtained using milder conditions for the ion bombardment and with high-temperature annealing while the reconstructed surface is obtained for ion bombardment at higher kinetic energy and at lower annealing temperatures^{5,7,8}.

The relaxed structure of the stoichiometric surface has $\text{Cu}_{\text{CUS}}\text{-O}$ and $\text{Cu}_{\text{CSA}}\text{-O}_{\text{CUS}}$ bond lengths of about 1.90 \AA and 1.81 \AA , which are longer and shorter, respectively, compared to Cu-O bonds in bulk Cu_2O (see Table I). The formation of a neutral oxygen vacancy ($\text{V}_\text{O}^\bullet$ in Kröger-Vink notation²¹) due to removal of one O_{CUS} from the stoichiometric $(\sqrt{3} \times \sqrt{3})\text{R}30^\circ$ surface results in a vacant site surrounded by three singly coordinated Cu ions (Cu_{NN} , see Fig. 1c) and leads to large structural relaxations: Cu_{NN} move towards the $\text{V}_\text{O}^\bullet$, forming

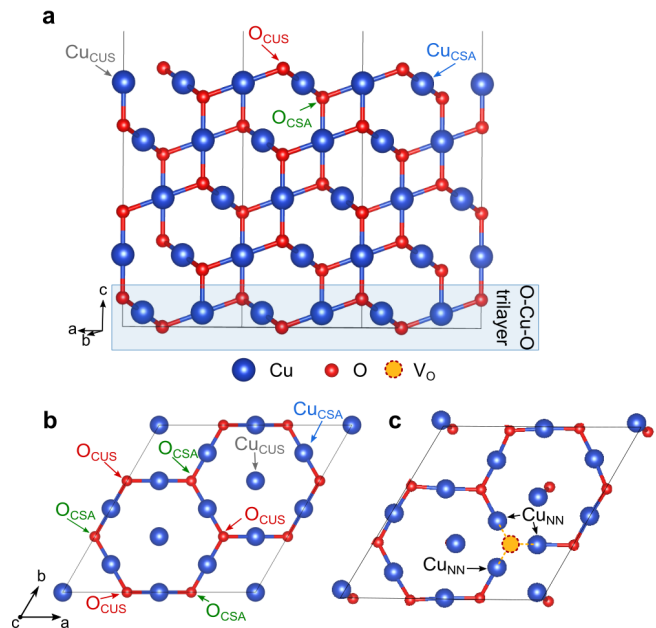


FIG. 1. a) Lateral and b) top view of the stoichiometric, unreconstructed (1×1) -(111) Cu_2O slab model within the $(\sqrt{3} \times \sqrt{3})\text{R}30^\circ$ supercell. O_{CUS} , Cu_{CUS} are the coordinatively unsaturated O and Cu surface sites, respectively, while O_{CSA} , and Cu_{CSA} indicate the coordinatively saturated O and Cu atoms. c) Top view of the reconstructed $(\sqrt{3} \times \sqrt{3})\text{R}30^\circ$ -(111) Cu_2O slab model with one oxygen vacancy (V_O). Cu_{NN} are Cu sites adjacent to V_O .

TABLE I. Interatomic distances on the reconstructed surface with neutral ($\text{V}_\text{O}^\bullet$), singly ($\text{V}_\text{O}^\bullet$) or doubly ($\text{V}_\text{O}^{\times}$) positively charged V_O , compared to the stoichiometric surface and bulk Cu_2O . See Fig. 1 for atomic labels.

Distance	$\text{V}_\text{O}^{\bullet\bullet}$ (Å)	$\text{V}_\text{O}^\bullet$ (Å)	$\text{V}_\text{O}^{\times}$ (Å)	Ideal (Å)	Bulk (Å)
$\text{Cu}_{\text{NN}}\text{-Cu}_{\text{NN}}$	2.47	2.47	2.47	3.01	3.01
$\text{Cu}_{\text{NN}}\text{-O}_{\text{CSA}}$	1.93	1.94	1.94	1.86	1.85
$\text{Cu}_{\text{CSA}}\text{-O}_{\text{CUS}}$	-	-	-	1.81	1.85
$\text{Cu}_{\text{CUS}}\text{-O}_{\text{CSA}}$	1.92	1.92	1.92	1.90	1.85
$\text{Cu}_{\text{CUS}}\text{-Cu}_{\text{NN}}$	2.54	2.64	2.58	3.01	3.01

a cluster of Cu ions with $\text{Cu}_{\text{NN}}\text{-Cu}_{\text{NN}}$ distances of about 2.47 \AA and at the same time, the Cu_{CUS} ions also move towards the defect, resulting in $\text{Cu}_{\text{CUS}}\text{-Cu}_{\text{NN}}$ distances of about 2.54 \AA , in both cases much shorter than the Cu-Cu bond lengths in the bulk (3.01 \AA , see Table I). This picture is in disagreement with semi-local DFT results that report $\text{V}_\text{O}^\bullet$ formation not to cause appreciable distortions in the surface structure^{9,11}, but it is in line with DFT+ U results¹⁰. The formation of charged V_O was, however, not taken into account in these studies. We find that the singly positively ($\text{V}_\text{O}^\bullet$) and doubly positively ($\text{V}_\text{O}^{\times}$) charged vacancies result in structural relaxations similar to $\text{V}_\text{O}^\bullet$, even though the distance between Cu_{CUS} and Cu_{NN} is slightly larger compared to $\text{V}_\text{O}^\bullet$ (see Table I and Fig. 1c).

Figure 2a illustrates the electronic properties of the

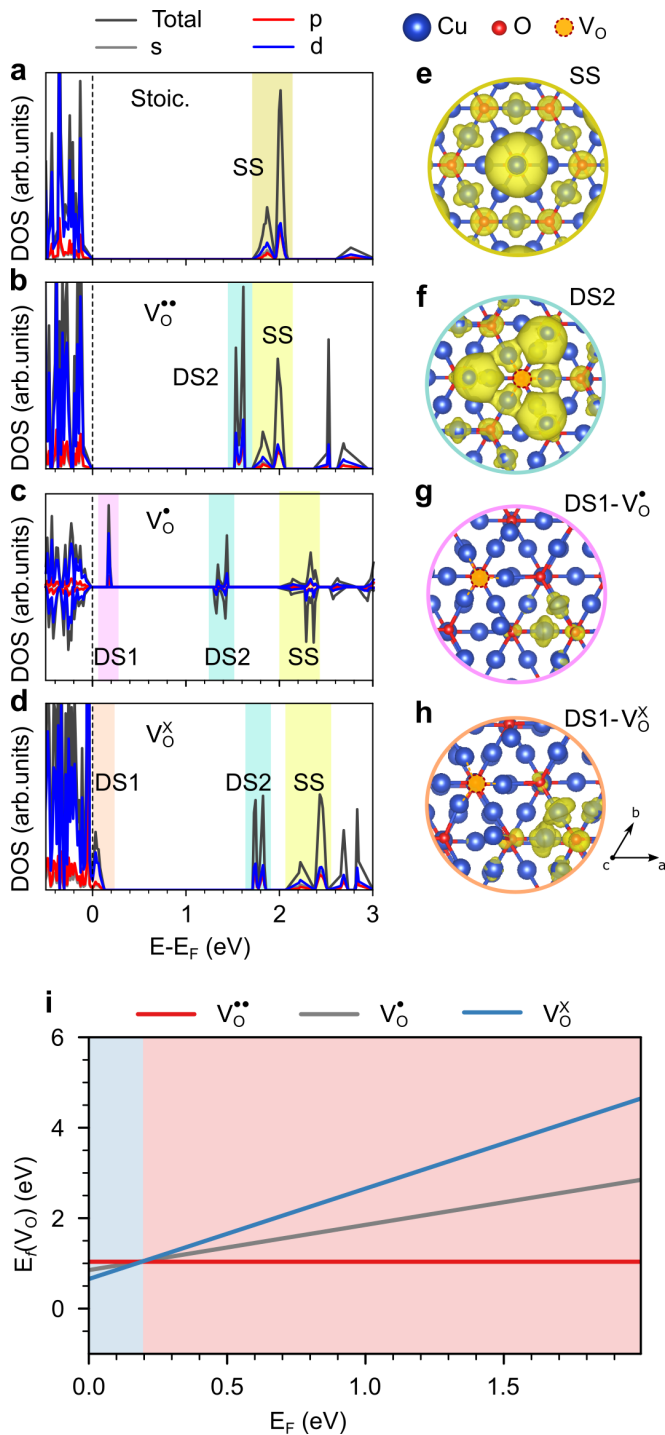


FIG. 2. Density of states for the $(\sqrt{3} \times \sqrt{3})R30^\circ$ supercell a) in the stoichiometric case and with one b) $V_O^{\bullet\bullet}$, c) V_O^\bullet , and d) V_O^X . The zero of the energy scale was set at the Fermi energy. For the spin-polarized V_O^\bullet calculation, the DOS for the spin-up and spin-down channels are reported with positive and negative values respectively on the y -axis. The isosurfaces ($2 \times 10^{-2} e/\text{\AA}^3$) in e-i) correspond to the charge density associated with the defect states (DS) or surface states (SS) highlighted with the corresponding color in plots a-d). i) Oxygen vacancy formation energy ($E_f(V_O)$) under O-poor conditions in different charge states as a function of the Fermi energy ranging from the valence band maximum ($E_F = 0$) up to the experimental band gap for the Cu_2O -(111) surface.

stoichiometric non-reconstructed Cu_2O (111) surface: in agreement with scanning tunneling spectroscopy (STS)^{7,11} and photoemission⁵ the band gap is significantly smaller than in bulk Cu_2O . This is due to the appearance of a peak at about 1.78 eV from the valence band maximum (VBM) that can be attributed to surface states localized mainly on Cu_{CUS} and Cu_{CSA} atoms in the outermost O–Cu–O trilayer (see Fig. 2e).

On the oxygen deficient reconstructed surface, a $V_O^{\bullet\bullet}$ results in the two excess electrons occupying states resonant with the valence band (VB, see Fig. 2b) and in the appearance of an empty localized defect state (DS2 in Fig. 2b) below the surface states (about 1.61 eV from VBM). DS2 has contributions of the three Cu_{NN} and the three Cu_{CUS} atoms closest to the oxygen vacancy (see Fig. 2f). If one oxygen atom and one electron are simultaneously removed to form V_O^\bullet , the extra electron occupies states resonant with the VB, while an unoccupied defect state appears at 0.17 eV, mainly localized on two Cu atoms far from the V_O^\bullet (DS1 in Fig. 2c and g), similar to what we observe for bulk Cu_2O (SI Fig. S4). Furthermore, in presence of V_O^\bullet , DS2 is stabilized and appears at about 1.3–1.4 eV in the gap, while the surface states are pushed up beyond 2.0 eV just below the conduction band (CB). Finally, V_O^X is associated with the empty defect state DS1 merged with the top of the VB and mainly localized on Cu atoms far away from the defect (see Fig. 2d and h). The splitting between the DS2 and surface states is still visible, but the corresponding peaks appear at about 1.8 and 2.1 eV, respectively, the highest ones being merged with the CB.

Figure 2i shows the formation energies of these surface V_O in the different charge states as a function of the position of the Fermi energy under O-poor conditions. The neutral defect has a formation energy of about 1.2 eV, slightly lower than previously reported using standard DFT functionals (1.4–1.7 eV)^{9–11}. As in the bulk (see SI Section S2), the neutral defect is most stable, except for Fermi energies just above the VBM, where V_O^X becomes the favored charge state with a thermodynamic transition level $\epsilon(+2/+1)$ of 0.20 eV. This confirms the existence of doubly charged V_O^X under p -type doping, leading to the $(\sqrt{3} \times \sqrt{3})\text{-}R30^\circ$ reconstruction. These vacancies strongly repel each other, simple electrostatic point-charge calculations suggesting energies larger by 4.5 eV for arrangements other than the ordered reconstruction.

B. Carrier Capture

Bulk calculations performed with better converged parameters compared to previous HSE calculations show that a thermodynamic transition level $\epsilon(0/+1)$ exists close to the valence band edge (see SI Section S3). Bulk oxygen vacancies could therefore, in principle, trap holes, while electron trapping is not possible. The computed hole-capture coefficient (see SI Section S4) is, however, very small, demonstrating that neither electron nor hole

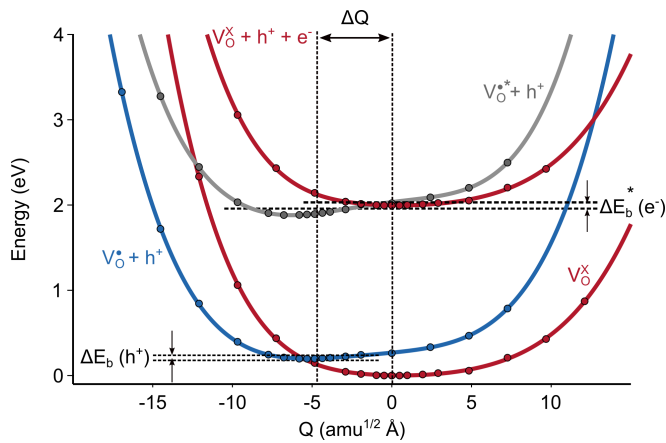


FIG. 3. Configuration coordinate diagram for $V_{\text{O}}(+2/+1)$ carrier capture at the reconstructed Cu_2O -(111) surface. The solid circles represent the relative formation energies calculated using hybrid DFT and lines are spline fits. ΔE_{b} are carrier capture barriers.

TABLE II. Key parameters for carrier capture processes at the reconstructed Cu_2O (111) surface: total mass-weighted distortions (ΔQ , in $\text{amu}^{1/2}\text{\AA}$), ionization energy (ΔE , in eV), carrier capture barrier (ΔE_{b} , in eV), carrier capture coefficient (C , in cm^3/s) and carrier capture cross section (σ in \AA^2) at 298 K.

Defect	Carrier	ΔQ	ΔE	ΔE_{b}	C	σ
$(+2/+1)$	h^+	4.83	0.20	0.003	1.24×10^{-19}	7.87×10^{-11}
$(+2/+1^*)$	e^-	4.83	2.00	0.011	4.87×10^{-9}	3.82

trapping by bulk V_{O} is likely.

The calculated 1D configuration coordinate diagram for carrier capture at the reconstructed $(\sqrt{3} \times \sqrt{3})\text{-R}30^\circ$ -(111) surface (Fig. 3) shows a very flat potential energy landscape for both the ground and excited states. The ground state is the doubly charged V_{O}^{X} , while for the excited state we initially consider the singly charged $V_{\text{O}}^{\bullet} + h^+$ with a hole in the VB. The minima of this ground and excited state are horizontally offset by $\Delta Q = 4.83 \text{ amu}^{1/2}\text{\AA}$ (see Table II), due to the large relaxations involving in particular the Cu_{CUS} (see Table I), while the energy difference between the two minima is only 0.20 eV, corresponding to the $\epsilon(+2/+1)$ charge transition level. The flat landscape and the large lattice relaxations result in a small hole capture barrier since the two curves intersect only 0.003 eV above the minimum of $V_{\text{O}}^{\bullet} + h^+$. This results in a hole-capture coefficient $C = 1.24 \times 10^{-19} \text{ cm}^3/\text{s}$ and hole-capture cross section $\sigma = 7.87 \times 10^{-11} \text{ \AA}^2$ at 298 K (see SI Fig. S6 for temperature-dependent values). While the potential energy curves of $V_{\text{O}}^{\text{X}} + h^+ + e^-$ and $V_{\text{O}}^{\bullet} + h^+$ intersect, the electron-capture barrier in excess of 2 eV will, given the inverse exponential dependence, result in a very small non-radiative electron capture rate.

Excited states of defects are believed to play a pivotal role in multiphonon emission processes in wide-gap

materials²². For a V_{O}^{\bullet} on the reconstructed surface, a spin-conserving excited state is reached by excitation of the extra electron from defect state DS1 to DS2 of the singly charged vacancy (see Fig. 2c). Beyond-DFT methods would, in principle, be necessary to describe excited states, but Alkauskas *et al.*²² showed that, for hybrid DFT functionals, accurate results can be obtained by approximating total energy differences by differences in single-particle Kohn-Sham eigenvalues in the spirit of the generalized Koopmans' theorem: at fixed geometry, the total energy of the excited state for a singly charged defect ($V_{\text{O}}^{\bullet*}$) is higher than that of the ground state V_{O}^{\bullet} by the eigenvalue difference between DS2 and DS1 evaluated for the ionized V_{O}^{X} state

$$E_{\text{tot},V_{\text{O}}^{\bullet*}} = E_{\text{tot},V_{\text{O}}^{\bullet}} + \epsilon_{\text{DS2},V_{\text{O}}^{\text{X}}} - \epsilon_{\text{DS1},V_{\text{O}}^{\text{X}}}, \quad (1)$$

where all terms are consistently calculated for the same geometry. As shown in Fig. 3, when this excited state is taken into account, electron capture into $V_{\text{O}}^{\bullet*}$ can occur because the $(+2/+1^*)$ transition lies closer to the CBM by the intradefect excitation energy of about 2.0 eV. The resulting electron-capture barrier of 0.011 eV and the proximity of the excited state to the CB lead to a large capture coefficient $C = 4.87 \times 10^{-9} \text{ cm}^3/\text{s}$ and cross section $\sigma = 3.87 \text{ \AA}^2$ at 298 K (see SI Fig. S6 for temperature-dependent values). Considering a defect density of $4.58 \times 10^{21} \text{ cm}^{-3}$ (one defect per supercell within 1 nm from the surface), this electron-capture coefficient results in an electron lifetime in the CB of about $4.47 \times 10^{-14} \text{ s}$ and a mean free path of $5.71 \times 10^{-07} \text{ cm}$. After the capture process the system can quickly relax from $V_{\text{O}}^{\bullet*}$ to V_{O}^{\bullet} via intradefect relaxations, the extra electron occupying either DS1 or DS2. This electron-capture process is represented in Fig. 4.

This mechanism for electron capture can be confirmed comparing the theoretical results with the electron dynamics at the (111) surface of Cu_2O experimentally determined via time-resolved 2PPE⁵. In these experiments, electrons are excited from the VB to the CB by absorption of a 3 eV laser pulse. The energy distribution of photoexcited electrons above the Fermi energy is monitored by a 6 eV laser pulse as function of the time delay between both pulses. In addition, valence band spectra were measured using ultraviolet photoelectron spectroscopy with He I_{α} radiation (21.2 eV). In Fig. 5 the measured valence and conduction band spectra are shown together with the computed DOS for both surfaces. On the stoichiometric (1×1) surface, the surface and low-lying conduction band states at 1.9 eV and 2.6 eV above the VBM are present, in good agreement with the computed DOS. The lifetime of excited electrons in the CB was determined as 10 ps. However, for the reconstructed $(\sqrt{3} \times \sqrt{3})\text{-R}30^\circ$ surface no photoemission signal from the CB is observed, but an intense defect state at 0.1 eV and another weaker state at 0.9 eV dominate the spectra. The missing photoemission signal from the CB is evidence for an ultrafast capture of photoexcited electrons by defects on the reconstructed surface. Occupation of those defect states by the excited

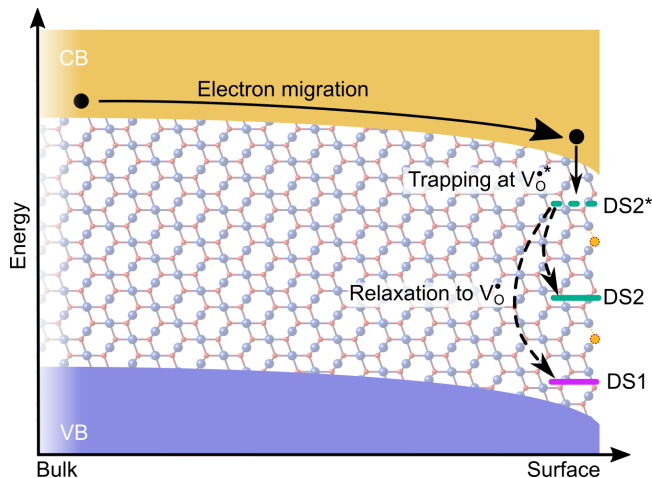


FIG. 4. Schematic representation of electron capture at the reconstructed $(\sqrt{3} \times \sqrt{3})R30^\circ$ Cu_2O -(111) surface. Due to surface band bending photo-excited electrons drift towards the surface, where they can either drive photocatalytic reactions (not shown) or be trapped in surface defect states (DS), if available. DS shown in the schematic result from experimentally observed surface oxygen vacancies (V_{O}). Direct trapping into DS1 or DS2 is slow, but an electron can very rapidly be trapped into an excited state DS2^* , from where it can relax into either DS1 or DS2. Blue and red spheres represents Cu and O atoms, respectively, while V_{O} are shown in orange.

electrons is faster than filling the low-lying CB states (0.030 ps) in good agreement with the electron lifetime in the CB predicted by DFT. These defects act as traps, since no noticeable decay of their electron population is observed over a time scale of hundreds of picoseconds. The good agreement between the experimental spectrum obtained in the 2PPE by populating the ground state V_{O}^{\times} with one extra electron and the computed density of states for the reconstructed surface with V_{O}^{\bullet} with in Fig. 5 confirms the predominance of charged oxygen vacancies in the $(\sqrt{3} \times \sqrt{3})$ - $R30^\circ$ reconstruction of the Cu_2O (111) surface, as well as the crucial role of the $V_{\text{O}}^{\times}/V_{\text{O}}^{\bullet}$ transition for the observed efficient electron-capture at this surfaces.

III. CONCLUSIONS

In summary, our hybrid DFT results show that bulk defects in Cu_2O cannot trap electrons and are highly inefficient hole traps. We further confirm that the $(\sqrt{3} \times \sqrt{3})$ - $R30^\circ$ reconstruction experimentally observed under oxygen-poor conditions on the Cu_2O (111) surface is associated with a $1/3$ monolayer of charged oxygen vacancies, as previously hypothesized based on experiments. We report an excellent agreement between experimental spectra and computed densities of states that confirm the singly charged (V_{O}^{\bullet}) state of these defects after electron trapping, and hence support the computed

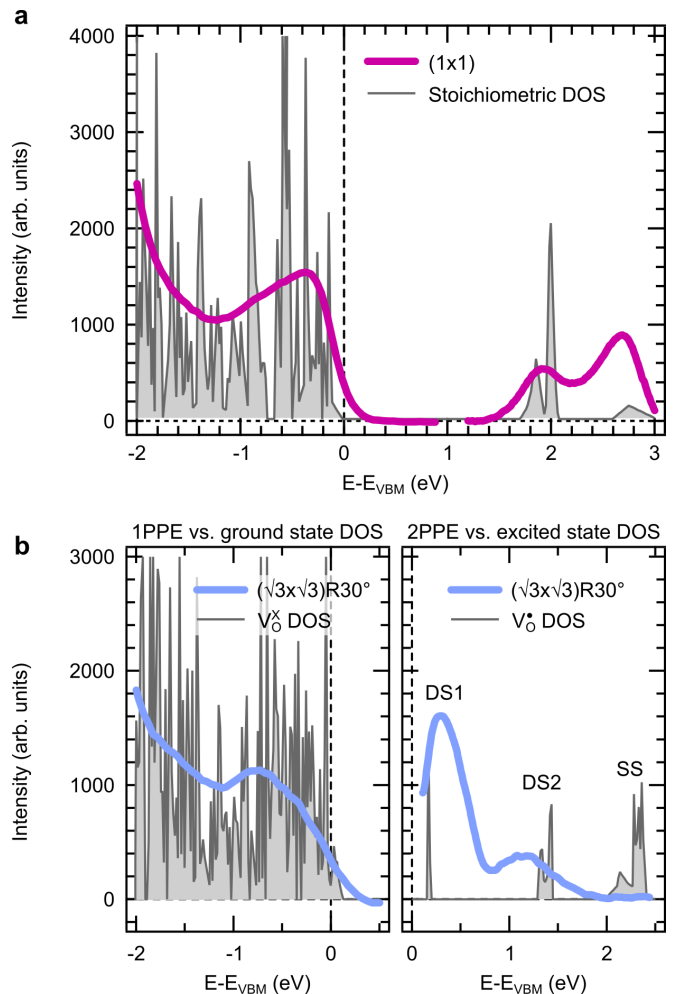


FIG. 5. Comparison of the experimentally measured (dashed lines) and computed (solid lines) density of states for a) the stoichiometric (1×1) and b) the reconstructed $(\sqrt{3} \times \sqrt{3})$ - $R30^\circ$ -(111) Cu_2O surface with V_{O} . For the valence band, determined using 1PPE, we compare with the ground-state V_{O}^{\times} DOS, whereas for the empty states, determined using 2PPE, we compare with the excited-state V_{O}^{\bullet} DOS. For the spin-polarized V_{O}^{\bullet} DOS, the spin-up and spin-down channels have been summed. Note the missing photoelectron signals at energies higher than 2 eV in (b).

doubly charged V_{O}^{\times} ground-state. Due to electrostatic repulsion, these defects form a highly ordered structure that strongly suppresses electron transport. In particular, the excited state of the V_{O}^{\bullet} plays a crucial role in efficient electron capture at the surface. Electrons are trapped by a transition from V_{O}^{\times} to the excited state $V_{\text{O}}^{\bullet*}$. After the capture process, the system can relax to V_{O}^{\bullet} via intradefect relaxation, the electron finally being trapped in the defect states associated with the singly charged defect. This process is predicted to have a capture coefficient of about $10^{-9} \text{ cm}^3/\text{s}$ leading to a free-carrier lifetime of 0.04 ps, in good agreement with experimental observations. The findings demonstrate the predominance of surface oxygen vacancies in limiting the

photocurrent of Cu₂O based heterostructures and provide a solid basis for the engineering of more efficient Cu₂O photoelectrodes.

ACKNOWLEDGMENTS

This work was funded by the Swiss National Science Foundation (grant numbers 200020_172641, PP00P2_157615 and PP00P2_187185). Computational resources for this work were provided by the University of Bern (on the HPC cluster UBELIX, <http://www.id.unibe.ch/hpc>) and by the Swiss National Supercomputing Center (CSCS) under project IDs s955 and s1033.

AUTHOR CONTRIBUTIONS

C.R. performed DFT calculations, L.G. performed experiments. C.R. and U.A. wrote the manuscript. All authors jointly analyzed the data and revised the manuscript.

COMPETING INTERESTS

The authors declare no competing interests.

IV. METHODS

All density functional theory (DFT) calculations were performed with the Vienna Ab-initio Simulation Package (VASP) ^{23–26}. The Heyd-Scuseria-Ernzerhof (HSE) ^{27,28} hybrid exchange-correlation functional was employed together with the default VASP Cu and O projector augmented wave (PAW) potentials ^{29,30} with Cu(4s, 3d) and O(2s, 2p) valence configurations. Wavefunctions were expanded in planewaves up to a kinetic energy of 500 eV. This setup provides an excellent agreement with experiment (see SI Sections [S1 A](#) and [S2](#)).

Surface calculations were performed using a ($\sqrt{3} \times \sqrt{3}$)R30° supercell of the ideal O-terminated (111) surface from which one surface O atom was removed, corresponding to a $\frac{1}{3}$ V_O monolayer. The slab model consists of five O-Cu-O trilayers with a 10 Å vacuum gap to prevent interactions between periodic images along the surface normal. The Brillouin zone of this slab model was sampled using a $3 \times 3 \times 1$ k-point mesh. Different charge states for the V_O were studied by adjusting the number of electrons and by applying a neutralizing background charge, as required by calculations under periodic-boundary conditions to avoid a divergence of the electrostatic potential. Atomic positions were optimized while keeping the lattice vectors fixed at optimized values of the non-defective system. Additionally, the atoms

in the bottom two trilayers were kept fixed at bulk positions. Structural relaxations were performed until forces converged below 10^{-3} eV/Å.

The formation energy of a V_O in a charge state q (E_{f,V_O^q}) was calculated as described in Ref. [31](#):

$$E_{f,V_O^q} = E_{tot,V_O^q} - E_{tot,stoich} + n_O\mu_O + q[E_{VBM} + E_F] + E_{corr} \quad (2)$$

where E_{tot,V_O^q} and $E_{tot,stoich}$ are the total energies of the defective and stoichiometric supercells, respectively, and E_F is the Fermi energy relative to the valence band maximum (E_{VBM}) of the stoichiometric cell, which can assume values within the band gap E_g ($0 \leq E_F \leq E_g$) of the non-defective structure. The third term includes the number of removed O atoms ($n_O < 0$) and the oxygen chemical potential μ_O . Results are reported for oxygen-poor conditions: $\mu_O = \frac{1}{2}\mu_{O_2} + \Delta\mu_O$, where μ_{O_2} is the energy of the O₂ molecule and $\Delta\mu_O = -1.55$ eV (see SI Section [S1 B](#) for details). Lastly, E_{corr} is a corrective term necessary to align the electrostatic potentials of the charged defective and the neutral stoichiometric cell obtained by averaging the electrostatic potential in spheres around atomic sites located far from the defect ³². No further finite-size corrections were applied since the defect concentration we simulate is realistic for this surface.

The thermodynamic transition level $\epsilon(q_1/q_2)$ for V_O defects with charge states q_1 and q_2 was computed as the Fermi level for which the formation energies of the two charge states are equal ³¹:

$$\epsilon(q_1/q_2) = \frac{E_{f,V_O^{q_1}}(E_F = 0) - E_{f,V_O^{q_2}}(E_F = 0)}{q_2 - q_1} \quad (3)$$

where E_{f,V_O^q} is the formation energy of a V_O in a charge state q in its equilibrium structure when the Fermi level is at the valence-band maximum ($E_F = 0$). For Fermi-level positions below $\epsilon(q_1/q_2)$, charge state q_1 is stable, while for Fermi-level positions above $\epsilon(q_1/q_2)$, charge state q_2 is stable.

We computed surface energies via *ab initio* atomistic thermodynamics, as shown for Cu₂O surfaces in Ref. [10](#):

$$\gamma = \frac{1}{2A} [E_{slab} - N_{Cu}\mu_{Cu} - N_O\mu_O], \quad (4)$$

where E_{slab} is the total energy of the slab, N_{Cu}/N_O are the number of Cu/O atoms in the model and μ_{Cu}/μ_O are the Cu/O chemical potentials. A is the surface area and the 1/2 factor accounts for the two surfaces contained in the slab. Results are reported for O-rich ($\Delta\mu_O = -1.41$ eV and $\Delta\mu_{Cu} = -0.07$ eV) and O-poor conditions ($\Delta\mu_{Cu} = 0$ and $\Delta\mu_O = -1.55$ eV, see SI Sections [S1 B](#) for details).

We considered non-radiative carrier capture processes involving a defect and occurring via multi-phonon emission ^{33,34}. Such processes can be described in DFT using the approach introduced by Alkauskas *et al.* ^{22,35} based on the static approximation ³⁶ and using an effective

one-dimensional configuration coordinate Q to represent the phonon wavefunction of all vibrations coupling to the change of the defect geometry upon carrier capture. Within this approach, the capture coefficient is

$$C(T) = sV\eta_{sp}g\frac{2\pi}{\hbar}W_{if}^2\sum_{m,n}w_m(T)|\langle\chi_{im}|Q+\Delta Q|\chi_{fn}\rangle|^2 \times \delta(\Delta E + \epsilon_{im} - \epsilon_{fn}), \quad (5)$$

where V is the volume of the supercell, η_{sp} accounts for spin-selection rules ($\eta_{sp} = 1/2$ when the initial state is a spin doublet and the final state is a spin singlet), g is the degeneracy of the final state, W_{if} is the electron-phonon coupling matrix element of the initial and final states, ΔE is the energy difference between the two states, χ and ϵ are the phonon wave functions and eigenvalues, respectively, for the excited (im) and ground (fn) electronic

states, while w_m is the thermal occupation number of the excited vibrational state. δ is replaced with a Gaussian function of finite width. Matrix elements W_{if} are computed according to Ref.³⁵ using the PAWpySeed package³⁷ to obtain the wavefunction overlap. The Sommerfeld factor s was computed according to Ref.^{38,39}, requiring electron and hole effective masses, obtained by finite differences as implemented in EMC⁴⁰. Non-radiative capture coefficients were calculated with the CarrierCapture.jl package⁴¹. Additional information can be found in SI Section S1C.

DATA AVAILABILITY

Data associated with the calculations is available on the Materials Cloud: <https://doi.org/10.24435/materialscloud:rr-2n>.

-
- ¹ B. K. Meyer, A. Polity, D. Reppin, M. Becker, P. Herzig, P. J. Klar, Th. Sander, C. Reindl, J. Benz, M. Eickhoff, C. Heiliger, M. Heinemann, J. Bläsing, A. Krost, S. Shokovets, C. Müller, and C. Ronning, “Binary Copper Oxide Semiconductors: From Materials towards Devices,” *Phys. Status Solidi (B)* **249**, 1487–1509 (2012).
 - ² W. Niu, T. Moehl, W. Cui, R. Wick-Joliat, L. Zhu, and S. D. Tilley, “Extended Light Harvesting with Dual Cu₂O-based Photocathodes for High Efficiency Water Splitting,” *Adv. Energy Mater.* **8**, 1702323 (2018).
 - ³ L. Pan, J. H. Kim, M. T. Mayer, M.-K. Son, A. Ummadisingu, J. S. Lee, A. Hagfeldt, J. Luo, and M. Grätzel, “Boosting the Performance of Cu₂O Photocathodes for Unassisted Solar Water Splitting Devices,” *Nat. Catal.* **1**, 412–420 (2018).
 - ⁴ M. Borgwardt, S. Omelchenko, M. Favaro, P. Plate, C. Höhn, D. Abou-Ras, K. Schwarzburg, R. Van de Krol, H. Atwater, N. Lewis, R. Eichberger, and D. Friedrich, “Femtosecond Time-Resolved Two-Photon Photoemission Studies of Ultrafast Carrier Relaxation in Cu₂O Photoelectrodes,” *Nat. Commun.* **10**, 1–7 (2019).
 - ⁵ L. Grad, Z. Novotny, M. Hengsberger, and J. Osterwalder, “Influence of Surface Defect Density on the Ultrafast Hot Carrier Relaxation and Transport in Cu₂O Photoelectrodes,” *Sci. Rep.* **10**, 1–10 (2020).
 - ⁶ K. H. Schulz and D. F. Cox, “Photoemission and Low-Energy-Electron-Diffraction Study of Clean and Oxygen-Dosed Cu₂O (111) and (100) Surfaces,” *Phys. Rev. B* **43**, 1610–1621 (1991).
 - ⁷ A. Önsten, M. Göthelid, and U. O. Karlsson, “Atomic Structure of Cu₂O(111),” *Surf. Sci.* **603**, 257–264 (2009).
 - ⁸ A. Önsten, J. Weissenrieder, D. Stoltz, S. Yu, M. Göthelid, and U. O. Karlsson, “Role of Defects in Surface Chemistry on Cu₂O(111),” *J. Phys. Chem. C* **117**, 19357–19364 (2013).
 - ⁹ B.-Z. Sun, W.-K. Chen, J.-D. Zheng, and C.-H. Lu, “Roles of Oxygen Vacancy in the Adsorption Properties of CO and NO on Cu₂O(111) surface: Results of a First-Principles Study,” *Appl. Surf. Sci.* **255**, 3141–3148 (2008).
 - ¹⁰ L. Isseroff Bendavid and E. A. Carter, “First-Principles Predictions of the Structure, Stability, and Photocatalytic Potential of Cu₂O surfaces,” *J. Phys. Chem. B* **117**, 15750–15760 (2013).
 - ¹¹ R. Zhang, L. Li, L. Frazer, K. B. Chang, K. R. Poepelmeier, M. K. Y. Chan, and J. R. Guest, “Atomistic Determination of the Surface Structure of Cu₂O(111): Experiment and Theory,” *Phys. Chem. Chem. Phys.* **20**, 27456–27463 (2018).
 - ¹² X. Yu, C. Zhao, T. Zhang, and Z. Liu, “Molecular and Dissociative O₂ adsorption on the Cu₂O(111) Surface,” *Phys. Chem. Chem. Phys.* **20**, 20352–20362 (2018).
 - ¹³ A. Gloystein, N. Nilius, J. Goniakowski, and C. Noguera, “Nanopyramidal Reconstruction of Cu₂O(111): A Long-Standing Surface Puzzle Solved by STM and DFT,” *J. Phys. Chem. C* **124**, 26937–26943 (2020).
 - ¹⁴ S. Koirala, M. Takahata, Y. Hazama, N. Naka, and K. Tanaka, “Relaxation of Localized Excitons by Phonon Emission at Oxygen Vacancies in Cu₂O,” *J. Lumin.* **155**, 65–69 (2014).
 - ¹⁵ M. Nolan and S. D. Elliott, “The p-type Conduction Mechanism in Cu₂O: a First Principles Study,” *Phys. Chem. Chem. Phys.* **8**, 5350–5358 (2006).
 - ¹⁶ H. Raebiger, S. Lany, and A. Zunger, “Origins of the p-type Nature and Cation Deficiency in Cu₂O and Related Materials,” *Phys. Rev. B* **76**, 045209 (2007).
 - ¹⁷ M. Nolan, “Defects in Cu₂O, CuAlO₂ and SrCu₂O₂ Transparent Conducting Oxides,” *Thin Solid Films* **516**, 8130–8135 (2008).
 - ¹⁸ D. O. Scanlon and G. W. Watson, “Undoped n-type Cu₂O: Fact or Fiction?” *J. Phys. Chem. Lett.* **1**, 2582–2585 (2010).
 - ¹⁹ B. Huang, “Intrinsic Deep Hole Trap Levels in Cu₂O with Self-Consistent Repulsive Coulomb Energy,” *Solid State Commun.* **230**, 49–53 (2016).
 - ²⁰ D. O. Scanlon, B. J. Morgan, G. W. Watson, and A. Walsh, “Acceptor Levels in p-Type Cu₂O: Rationalizing Theory and Experiment,” *Phys. Rev. Lett.* **103**, 096405 (2009).

- ²¹ F. A. Kröger and H. J. Vink, “Relations between the Concentrations of Imperfections in Crystalline Solids,” *Solid State Phys.* **3**, 307–435 (1956).
- ²² A. Alkauskas, C. E. Dreyer, J. L. Lyons, and C. G. Van de Walle, “Role of Excited States in Shockley-Read-Hall Recombination in Wide-Band-Gap Semiconductors,” *Phys. Rev. B* **93**, 201304 (2016).
- ²³ G. Kresse and J. Hafner, “Ab Initio Molecular Dynamics for Liquid Metals,” *Phys. Rev. B* **47**, 558–561 (1993).
- ²⁴ G. Kresse and J. Hafner, “Ab Initio Molecular-Dynamics Simulation of the Liquid-Metal–Amorphous-Semiconductor Transition in Germanium,” *Phys. Rev. B* **49**, 14251–14269 (1994).
- ²⁵ G. Kresse and J. Furthmüller, “Efficiency of ab-initio Total Energy Calculations for Metals and Semiconductors using a Plane-Wave Basis Set,” *Comput. Mater. Sci.* **6**, 15–50 (1996).
- ²⁶ G. Kresse and J. Furthmüller, “Efficient Iterative Schemes for Ab Initio Total-Energy Calculations using a Plane-Wave Basis Set,” *Phys. Rev. B* **54**, 11169–11186 (1996).
- ²⁷ J. Heyd, G. E. Scuseria, and M. Ernzerhof, “Hybrid Functionals Based on a Screened Coulomb Potential,” *J. Chem. Phys.* **118**, 8207–8215 (2003).
- ²⁸ J. Heyd and G. E. Scuseria, “Efficient Hybrid Density Functional Calculations in Solids: Assessment of the Heyd–Scuseria–Ernzerhof screened Coulomb Hybrid Functional,” *J. Chem. Phys.* **121**, 1187–1192 (2004).
- ²⁹ P. E. Blöchl, “Projector Augmented-Wave Method,” *Phys. Rev. B* **50**, 17953–17979 (1994).
- ³⁰ G. Kresse and D. Joubert, “From Ultrasoft Pseudopotentials to the Projector Augmented-Wave Method,” *Phys. Rev. B* **59**, 1758–1775 (1999).
- ³¹ C. Freysoldt, B. Grabowski, T. Hickel, J. Neugebauer, G. Kresse, A. Janotti, and C. G. Van de Walle, “First-Principles Calculations for Point Defects in Solids,” *Rev. Mod. Phys.* **86**, 253 (2014).
- ³² S. Lany and A. Zunger, “Assessment of Correction Methods for the Band-Gap Problem and for Finite-Size Effects in Supercell Defect Calculations: Case Studies for zno and GaAs,” *Phys. Rev. B* **78**, 235104 (2008).
- ³³ K. Huang, A. Rhys, and N. F. Mott, “Theory of Light Absorption and Non-Radiative Transitions in *F*-centres,” *Proc. R. Soc. Lond. Series A. Mathematical and Physical Sciences* **204**, 406–423 (1950).
- ³⁴ C. H. Henry and D. V. Lang, “Nonradiative Capture and Recombination by Multiphonon Emission in GaAs and GaP,” *Phys. Rev. B* **15**, 989–1016 (1977).
- ³⁵ A. Alkauskas, Q. Yan, and C. G. Van de Walle, “First-Principles Theory of Nonradiative Carrier Capture via Multiphonon Emission,” *Phys. Rev. B* **90**, 075202 (2014).
- ³⁶ H. Huang, “Adiabatic Approximation Theory and Static Coupling Theory of Nonradiative Transition,” *Sci. Sin.* **24**, 27–34 (1981).
- ³⁷ K. Bystrom, D. Broberg, S. Dwaraknath, K. A. Persson, and M. Asta, “Pawpyseed: Perturbation-Extrapolation Band Shifting Corrections for Point Defect Calculations,” (2019), [arXiv:1904.11572 \[cond-mat.mtrl-sci\]](https://arxiv.org/abs/1904.11572).
- ³⁸ S. Kim, J.-S. Park, S. N. Hood, and A. Walsh, “Lone-Pair Effect on Carrier Capture in Cu₂ZnSnS₄ Solar Cells,” *J. Mater. Chem. A* **7**, 2686–2693 (2019).
- ³⁹ S. Kim, J. A. Márquez, T. Unold, and A. Walsh, “Upper Limit to the Photovoltaic Efficiency of Imperfect Crystals from First Principles,” *Energy Environ. Sci.* **13**, 1481–1491 (2020).
- ⁴⁰ A. Fonari and C. Sutton, “Effective Mass Calculator,” (2012).
- ⁴¹ S. Kim, N. S. Hood, and A. Walsh, “Carriercapture,” <https://github.com/WMD-group/CarrierCapture.jl> (2019)

Supplementary information for

Importance of surface oxygen vacancies for ultrafast hot carrier relaxation and transport in Cu₂O

Chiara Ricca,^{1,2} Lisa Grad³, Matthias Hengsberger³, Jürg Osterwalder³, and Ulrich Aschauer^{1,2}

¹*Department of Chemistry and Biochemistry, University of Bern, Freiestrasse 3, CH-3012 Bern, Switzerland*

²*National Centre for Computational Design and Discovery of Novel Materials (MARVEL), Switzerland*

³*Department of Physics, University of Zurich, Winterthurerstrasse 190, CH-8057 Zurich, Switzerland*

(Dated: March 9, 2021)

S1. METHOD DETAILS

A. Bulk calculations

Cu₂O (cuprous oxide, mineral cuprite) has a cubic structure with four Cu and two O atoms in the unit cell (space group $Pn\bar{3}m$). A $2 \times 2 \times 2$ supercell of the 6-atom unit cell was used to model oxygen-deficient bulk cuprous oxide with a Γ -centered $6 \times 6 \times 6$ Monkhorst-Pack¹ \mathbf{k} -point grid to sample the Brillouin zone. Defects were created by removing one oxygen atom (V_O , concentration $\approx 6\%$) from this 48-atom supercell. For the stoichiometric bulk, both lattice parameters and atomic positions were allowed to relax, while for defect and surface calculations the lattice parameters are kept fixed at their relaxed bulk values. Structural relaxations were performed until forces converged below 10^{-3} eV/Å and stress components below 5×10^{-5} eV/Å³. Electrostatic corrections^{2,3} were considered for bulk defects using the experimental value of 7.1⁴ for the dielectric constant.

B. Cu₂O chemical potentials

When calculating oxygen vacancy formation energies, different synthesis conditions can be accounted for by adjusting the oxygen chemical potential ($\mu_O = \mu_O^0 + \Delta\mu_O$) assuming that it is in equilibrium with a given oxygen reservoir. If $\mu_O = \frac{1}{2}\mu(O_2) + \Delta\mu_O$, where $\mu(O_2)$ is the total energy of O₂ in its triplet state, then $\Delta\mu_O$ can vary within a range limited by the formation of CuO for the oxygen-rich limit and by the decomposition of Cu₂O to metallic Cu for the oxygen-poor limit. The first condition is given by

$$\Delta\mu_{Cu} + \Delta\mu_O = \Delta H_f^{CuO} = -1.48 \text{ eV}, \quad (S1)$$

where ΔH_f^{CuO} is the heat of formation of CuO computed at the HSE level of theory. The second condition is given by

$$\mu_{Cu} = \mu_{Cu;metal} \rightarrow \Delta\mu_{Cu} = 0 \quad (S2)$$

and since the chemical potentials are related by

$$2\Delta\mu_{Cu} + \Delta\mu_O = \Delta H_f^{Cu_2O} = -1.55 \text{ eV}, \quad (S3)$$

where $\Delta H_f^{Cu_2O}$ is the heat of formation of cuprous oxide computed with the HSE functional, this results in

$$\Delta\mu_O = -1.41 \text{ eV} \quad (S4)$$

$$\Delta\mu_{Cu} = -0.07 \text{ eV} \quad (S5)$$

and

$$\Delta\mu_O = -1.55 \text{ eV} \Delta\mu_{Cu} = 0.00 \text{ eV} \quad (S6)$$

for the O-rich and O-poor case, respectively.

C. Non-radiative carrier capture

We considered non-radiative carrier capture processes involving a defect and occurring via multi-phonon emission^{5,6}. In such a process, a system in an initial excited state (i), for example a neutral $V_{\text{O}}^{\bullet\bullet}$ in Cu_2O with a hole (h^+) in the valence band, vibrates around its equilibrium geometry. Because of electron-phonon coupling, the deformation of the structure induces oscillations in the electronic energy level of the defect state, eventually allowing hole capture, *i.e.* an energy-conserving transition to the final electronic ground state (f) constituted by the singly positively charged V_{O}^{\bullet} , followed by the relaxation of the system towards the equilibrium geometry of the ground state by emitting multiple phonons. Such a process can be described by first principles using the approach introduced by Alkauskas *et al.*^{7,8} based on the static approximation⁹ and using an effective one-dimensional configuration coordinate Q to represent the phonon wavefunction describing all the vibrations coupling to the change of the defect's geometry caused by the carrier capture:

$$Q^2 = \sum_{\alpha,i} m_{\alpha} \Delta R_{\alpha,i}^2, \quad (\text{S7})$$

where m_{α} and $\Delta R_{\alpha,i}$ are the mass and the displacement of atom α from its equilibrium position in one of the two charge states along the i -direction. Within this approach, the capture coefficient is given by

$$C(T) = sV\eta_{sp}g \frac{2\pi}{\hbar} W_{if}^2 \sum_{m,n} w_m(T) |\langle \chi_{im} | Q + \Delta Q | \chi_{fn} \rangle|^2 \times \delta(\Delta E + \epsilon_{im} - \epsilon_{fn}), \quad (\text{S8})$$

where V is the volume of the supercell, η_{sp} accounts for spin-selection rules ($\eta_{sp} = 1/2$ when the initial state is a spin doublet and the final state is a spin singlet), g is the degeneracy of the final state, W_{if} is the electron-phonon coupling matrix element of the initial and final states, ΔE is the energy difference between the two states, χ and ϵ are the phonon wave functions and eigenvalues, respectively, for the excited (im) and ground (fn) electronic states, while w_m is the thermal occupation number of the excited vibrational state. δ is replaced with a Gaussian function with a finite width. Matrix elements W_{if} are computed according to Ref.⁷. The Sommerfeld factor s , computed as described in Ref.^{10,11}, is necessary to describe the capture by charged defects since it accounts for the Coulomb interaction at a temperature T between a carrier with charge q and a charged defect in a charge state Q :

$$s = \begin{cases} 4|Z|(\pi E_{\text{R}}/k_{\text{B}}T)^{1/2} & \text{for } Z < 0 \\ 8/\sqrt{3}(\pi^2 Z^2 E_{\text{R}}/k_{\text{B}}T)^{2/3} \exp(-3(Z^2 \pi^2 E_{\text{R}}/k_{\text{B}}T)^{1/3}) & \text{for } Z > 0 \end{cases} \quad (\text{S9})$$

where $Z = Q/q$ is negative for an attractive and positive for a repulsive center, k_{B} is the Boltzmann constant, $E_{\text{R}} = m^*q^4/(2\hbar^2\epsilon^2)$, with ϵ the dielectric constant of Cu_2O and m^* the carrier effective mass.

Carrier capture cross-sections (σ) are derived from $C(T) = \sigma(T)v(T)$, where v is the carrier thermal velocity $v(T) = \sqrt{3k_{\text{B}}T/m^*}$.

S2. STOICHIOMETRIC BULK Cu_2O

Cu_2O crystallizes in a simple cubic lattice (space group $Pn\bar{3}m$) with six atoms in the unit cell: four Cu positioned on a face-centered cubic lattice and the two O atoms occupying the tetrahedral sites and forming a body-centered cubic sub-lattice (see Fig. S1). Consequently, the copper atoms are linearly coordinated by two nearest neighbor O atoms (D_{3h} symmetry), while each oxygen is fourfold coordinated (T_d symmetry). As can be seen from Table S1, the structural parameters computed with the hybrid HSE functional are in excellent agreement with experiment (a mean absolute error of 0.4% on the lattice parameters and the Cu–O distance), in line with previous reports^{12–14}. In line with previous studies based on hybrid DFT^{12–15}, our predicted band gap is in excellent agreement with experiment, being underestimated by only 0.17 eV (see Table S1).

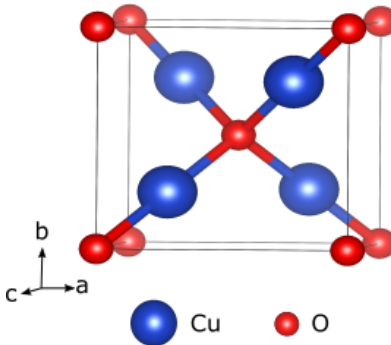


FIG. S1. $Pn\bar{3}m$ unit cell of Cu_2O .

TABLE S1. Comparison of the calculated and experimental structural properties (lattice parameters a in Å, Cu–O distance d in Å, and band gap E_g in eV).

	HSE	Expt.
a	4.288	4.270 ¹⁶
d	1.857	1.850 ¹⁶
E_g	2.00	2.17 ¹⁷

Figures S2 and S3 shows the predicted electronic structure of Cu_2O with the highest lying valence band (VB) states mainly formed by the antibonding Cu-3d states with a small admixing of O-2p states mainly contributing at lower energies in the VB. The bottom of the conduction is formed, instead, by Cu-4s and 3d states. The experimentally observed p -type behavior of cuprous oxide is a consequence of this peculiar electronic structure with the formally fully occupied Cu-3d states at the top of the VB, as opposed to the majority of oxides that show O-2p character for the highest lying VB states. Additionally, for a good p -type conductor, the VB should be highly dispersive leading to a low hole effective mass and thus high mobility¹⁸ (see Fig. S3).

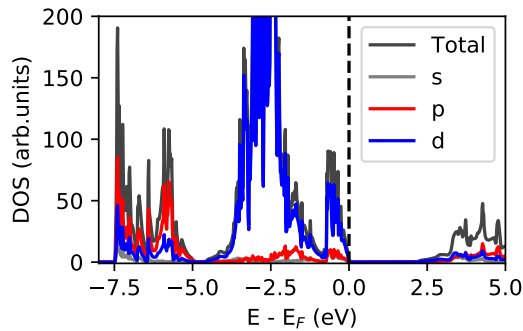


FIG. S2. Total and orbital-projected density of states (DOS and PDOS, respectively) for bulk Cu_2O computed at the HSE level of theory. The zero of the energy scale was set at the Fermi energy.

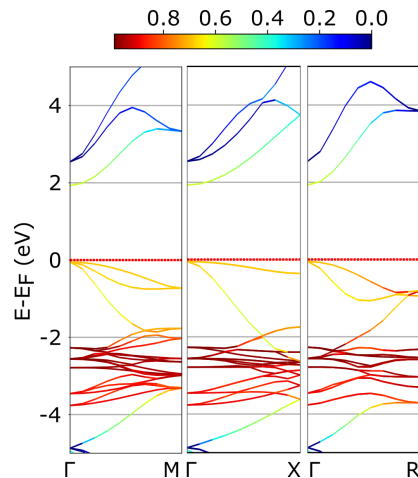


FIG. S3. Electronic bandstructure of Cu_2O computed at the HSE level. The contribution of the Cu-3d to the different bands is shown as coloured fat bands.

The electron and hole effective masses computed with HSE for Cu_2O along the high symmetry directions at the band extrema at Γ are reported in Table S2. In absence of spin-orbit splitting, the states at the VBM at Γ are triply degenerate and we can identify two heavy and one light hole band. The effective masses are isotropic, in line with experiments¹⁹. By averaging over the three degenerate bands, we obtain a conduction effective mass for the hole of $0.54m_0$. Our calculated effective masses are slightly smaller than the available experimental values. Our results, however, are different from the theoretical prediction of Nie *et al.*²⁰ who, while using only LDA, included spin-orbit interaction, which, mixing the wavefunctions at the top of VB, has a very large effect on the calculated effective masses and removes the degeneracy of the VBM, resulting in the light hole state becoming the top of the VB.

TABLE S2. Calculated electron and hole effective masses (in units of free electron mass m_0) at Γ . Results are compared with available experimental data.

	HSE				Average	Expt.
	[100]	[010]	[111]			
CBM	0.83	0.83	0.83		0.83	0.99 ²¹ , 0.98 ²²
VBM	0.20	0.20	0.20		0.54	0.58 ²¹ , 0.69 ²²
	3.89	3.88	3.88			
	3.89	3.89	3.88			

S3. DEFECTIVE BULK Cu_2O

The properties of oxygen vacancies (V_{O}) in cuprous oxide are still widely debated with contradictory results reported by both experiments^{23–30} and theory^{12,13,15,18,31–33}. Cu_2O predominantly has Schottky defects (O and Cu vacancy pairs) in concentrations determined by the synthesis temperature. Donor states in Cu_2O samples synthesized at oxygen partial pressures of $10^{-3} - 10^{-1}$ mmHg were reported for the first time in photoluminescence (PL) experiments²³, and attributed to singly and doubly ionized V_{O} . A donor level 0.38 eV below the CB minimum (CBM) and attributed to V_{O} was subsequently confirmed in PL spectra of electrodeposited cuprous oxide by different authors^{24–27}. In more recent PL studies, the broad luminescence bands at 1.72 eV and 1.53 eV from the VB were assigned to doubly and singly positively charged V_{O} , respectively^{28–30}, even though the exact position of the peaks and their relative intensity was found to strongly depend on the synthesis and post-processing conditions.

Early DFT results¹⁵ reported that under oxidizing conditions ($E_{\text{F}} = 0$ in Eq. 2 of the main text) the most stable V_{O} is in the +2 charge state. This result was obtained using the general gradient approximation (GGA) PBE exchange-correlation functional. A subsequent study, reported, however, a completely different behavior using the same functional: no donor level associated with V_{O} was observed inside the band gap, suggesting that V_{O} cannot act as a hole killer in cuprous oxide¹⁸. Similar conclusions were reached with the more accurate hybrid HSE functional^{12,13,32}. Discrepancies of theoretical results can be explained by different DFT functionals, but also by different corrections for charged defects in periodic supercells, and by computational details like the sampling of the Brillouin zone. The validity of earlier results^{12,13,32} obtained using a coarser \mathbf{k} -point sampling (presumably due to the high cost of HSE calculations and computational limitations at that time) was shown to lead to incorrect predictions for Cu vacancies in Cu_2O ³⁴. Given that more accurate calculations are now affordable, we repeated the study of V_{O} in Cu_2O using the HSE functional but with a denser \mathbf{k} -point mesh.

Figure S4 shows the computed density of states for a neutral, singly, and doubly positively charged V_{O} in bulk Cu_2O . These are designated in Kröger-Vink notation³⁵ as $V_{\text{O}}^{\bullet\bullet}$, V_{O}^{\bullet} , and V_{O}^{\times} respectively, where \bullet and \times superscripts indicate, respectively, a charge of +1 and 0 relative to the respective lattice site, h^+/e^- represent free holes/electrons, and a transition from $V_{\text{O}}^{\bullet} + e^-$ to $V_{\text{O}}^{\bullet\bullet}$ designates the electron capture process by a V_{O}^{\bullet} defect. The two extra electrons left in the lattice upon $V_{\text{O}}^{\bullet\bullet}$ formation are resonant in the VB (see Fig. S4a and d). If one oxygen atom and one electron are simultaneously removed to form V_{O}^{\bullet} , the defect state is split in a filled state still merged with the top of VB and occupied by the remaining extra electron, and an unoccupied state lying at 1.45 eV in the gap and mainly localized on two Cu atoms far from the V_{O} (see Fig. S4b and e). Finally, V_{O}^{\times} is associated with an empty defect state at about 1.53 eV localized on 4 Cu atoms in next nearest neighbor positions to the defect (see Fig. S4c and f). Structural relaxations observed upon defect formation are minimal and restricted to the four Cu atoms in nearest neighbor positions to V_{O} that move towards the vacancy, thus elongating their remaining Cu–O bonds by about 0.13 Å for $V_{\text{O}}^{\bullet\bullet}$ and V_{O}^{\times} and 0.14 Å for V_{O}^{\bullet} .

Figure S4g illustrates the changes in the formation energies for a V_{O} in the considered charge states as a function of the position of the Fermi energy under O-poor synthesis conditions. In agreement with previous results^{12,13,18,32}, $V_{\text{O}}^{\bullet\bullet}$ has a relatively low formation energy. However, we observe that for Fermi energies very close to the top of the valence band V_{O}^{\bullet} becomes the favored charge state. Thus, contrarily to previous results^{12,13,32} with the same hybrid DFT functional, but with a coarser \mathbf{k} -point grid, the computed thermodynamic transition level $\epsilon(+1/0)$ at 0.21 eV suggests that, under oxidizing conditions ($E_{\text{F}} = 0$ in eq. 2), V_{O} in Cu_2O could potentially act as hole traps, due to the proximity of the $\epsilon(+1/0)$ transition level to the VB, and hence to the low ionization energy for the $V_{\text{O}}^{\bullet}/V_{\text{O}}^{\bullet\bullet}$ couple.

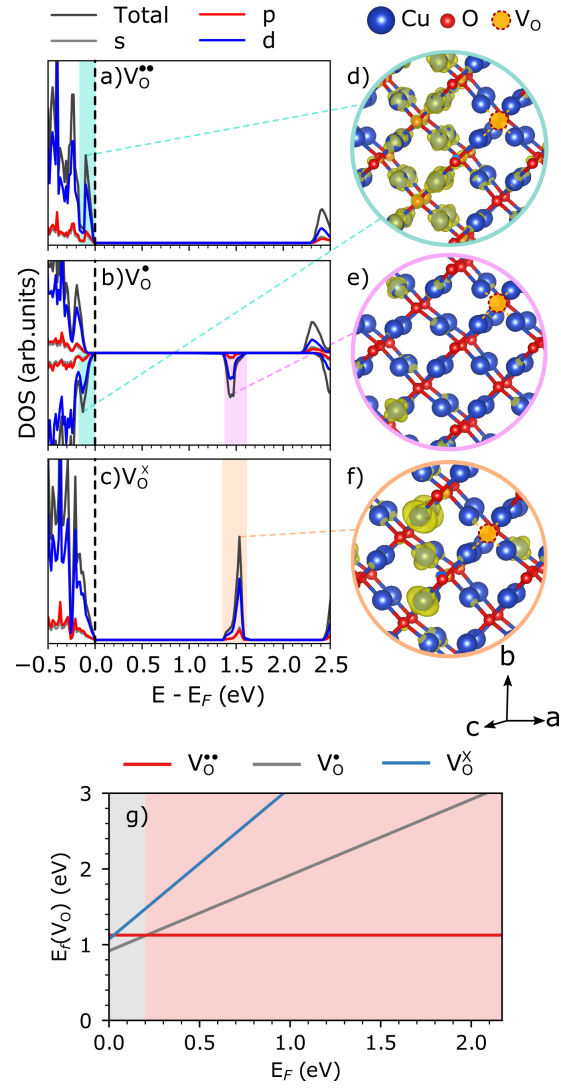


FIG. S4. Total and projected density of states for one a) $V_{\text{O}}^{\bullet\bullet}$, b) V_{O}^{\bullet} , and c) V_{O}^{\times} in bulk Cu_2O . The zero of the energy scale is at the Fermi energy. For the spin-polarized V_{O}^{\bullet} calculation, the DOS for the spin-up and spin-down channels are reported with positive and negative values along the y -axis. The isosurfaces ($2 \times 10^{-2} e/\text{\AA}^3$) in d)-f) show the charge density associated with the defect states highlighted with the corresponding color in panels a)-c). g) Oxygen vacancy formation energy ($E_f(V_{\text{O}})$) under O-poor conditions in different charge states as a function of the Fermi energy ranging from the valence band maximum ($E_F = 0$) up to the experimental band gap for stoichiometric bulk Cu_2O .

S4. CARRIER CAPTURE

The calculated 1D configuration coordinate diagram for carrier capture in bulk Cu_2O is shown in Fig. S5 with extracted key parameters in Table S3. The ground state is the V_{O}^{\bullet} defect, while the excited state corresponds to the neutral oxygen vacancy and a hole in the VB ($V_{\text{O}}^{\bullet\bullet} + h^+$). The separation between the minima of the two potential energy curves is $\Delta E = 0.21$ eV, corresponding to the charge transition level with respect to the VBM. The minima are offset horizontally by only $\Delta Q = 0.31$ $\text{amu}^{1/2}\text{\AA}$, in line with the minimal structural relaxations upon V_{O} formation in bulk Cu_2O . As a consequence, a sizable hole capture barrier $\Delta E_b = 1.685$ eV leads to a small hole capture coefficient $C = 1.04 \times 10^{-28}$ cm^3/s and hole capture cross-section $\sigma = 6.57 \times 10^{-20}$ \AA^2 at 298 K (for temperature-dependent values see SI Fig. S6). Electron capture, on the other hand, cannot happen since the $V_{\text{O}}^{\bullet\bullet} + h^+$ and $V_{\text{O}}^{\bullet} + h^+ + e^-$ curves in Fig. S5a do not intersect.

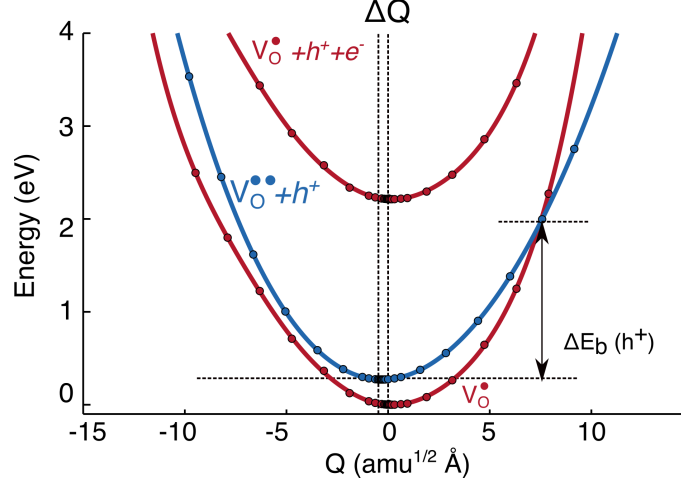


FIG. S5. Configuration coordinate diagram for carrier capture a) for $V_{\text{O}}(+/0)$ in bulk Cu_2O and b) for $V_{\text{O}}(+2/+1)$ at the reconstructed Cu_2O -(111) surface. The solid circles represent the relative formation energies calculated using hybrid DFT and the lines are spline fits. ΔE_b is the carrier capture barrier.

Table S3 reports additional key parameters involved in the carrier capture process compared to the table in the main text.

TABLE S3. Key parameters for the carrier capture process in the oxygen-deficient bulk cuprous oxide or at the reconstructed Cu_2O -(111) surface: degeneracy factor g of the final state, total mass-weighted distortions (ΔQ , in $\text{amu}^{1/2}\text{\AA}$), ionization energy (ΔE , in eV), carrier capture barrier (ΔE_b , in eV), electron-phonon coupling matrix element (W_{if} , in $\text{eV}/\text{amu}^{1/2}\text{\AA}$), and Sommerfeld factor (s), carrier capture coefficient (C , in cm^3/s) and carrier capture cross section (σ , \AA^2) at 298 K.

System	Defect	Carrier	g	ΔQ	ΔE	ΔE_b	W_{if}	s	C	σ
Bulk	(+/0)	holes	2	0.31	0.21	1.685	0.00039	7.2×10^{-4}	1.04×10^{-28}	6.57×10^{-20}
Surface	(+2/+1)	holes	3	4.83	0.20	0.003	0.00257	2.08×10^{-6}	1.24×10^{-19}	7.87×10^{-11}
	(+2/+1*)	electrons	3	4.83	2.00	0.011	0.00206	33.77	4.87×10^{-9}	3.82

Figure S6 reports the temperature dependent carrier capture coefficients in the bulk and at the reconstructed (111) surface.

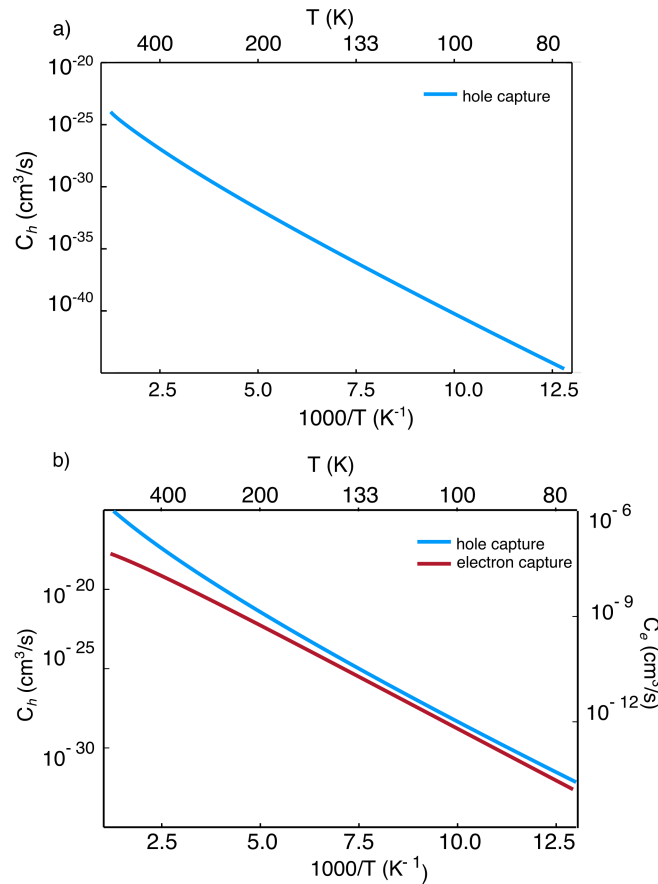


FIG. S6. Temperature dependence of the carrier capture coefficients computed for a) bulk Cu_2O or b) for the Cu_2O (111) surface.

-
- ¹ H. J. Monkhorst and J. D. Pack, *Phys. Rev. B* **13**, 5188 (1976).
 - ² G. Makov and M. C. Payne, *Phys. Rev. B* **51**, 4014 (1995).
 - ³ S. Lany and A. Zunger, *Model. Simul. Mater. Sci. Eng.* **17**, 084002 (2009).
 - ⁴ H. Stolz, F. Schöne, and D. Semkat, *New J. Phys.* **20**, 023019 (2018).
 - ⁵ K. Huang, A. Rhys, and N. F. Mott, *Proc. R. Soc. Lond. Series A. Mathematical and Physical Sciences* **204**, 406 (1950).
 - ⁶ C. H. Henry and D. V. Lang, *Phys. Rev. B* **15**, 989 (1977).
 - ⁷ A. Alkauskas, Q. Yan, and C. G. Van de Walle, *Phys. Rev. B* **90**, 075202 (2014).
 - ⁸ A. Alkauskas, C. E. Dreyer, J. L. Lyons, and C. G. Van de Walle, *Phys. Rev. B* **93**, 201304 (2016).
 - ⁹ H. Huang, *Sci. Sin.* **24**, 27 (1981).
 - ¹⁰ S. Kim, J.-S. Park, S. N. Hood, and A. Walsh, *J. Mater. Chem. A* **7**, 2686 (2019).
 - ¹¹ S. Kim, J. A. Márquez, T. Unold, and A. Walsh, *Energy Environ. Sci.* **13**, 1481 (2020).
 - ¹² D. O. Scanlon, B. J. Morgan, G. W. Watson, and A. Walsh, *Phys. Rev. Lett.* **103**, 096405 (2009).
 - ¹³ D. O. Scanlon and G. W. Watson, *J. Phys. Chem. Lett.* **1**, 2582 (2010).
 - ¹⁴ M. Heinemann, B. Eifert, and C. Heiliger, *Phys. Rev. B* **87**, 115111 (2013).
 - ¹⁵ M. Nolan and S. D. Elliott, *Phys. Chem. Chem. Phys.* **8**, 5350 (2006).
 - ¹⁶ A. Werner and H. D. Hochheimer, *Phys. Rev. B* **25**, 5929 (1982).
 - ¹⁷ *J. Am. Chem. Soc.* **130**, 382 (2008).
 - ¹⁸ H. Raebiger, S. Lany, and A. Zunger, *Phys. Rev. B* **76**, 045209 (2007).
 - ¹⁹ T. Ohyama, T. Ogawa, and H. Nakata, *Phys. Rev. B* **56**, 3871 (1997).
 - ²⁰ X. Nie, S.-H. Wei, and S. B. Zhang, *Phys. Rev. B* **65**, 075111 (2002).
 - ²¹ J. W. Hodby, T. E. Jenkins, C. Schwab, H. Tamura, and D. Trivich, *J. Phys. C. Solid State Phys.* **9**, 1429 (1976).

- ²² A. Goltzene, C. Schwab, and H. C. Wolf, *Solid State Commun.* **18**, 1565 (1976).
- ²³ J. Bloem, *Phillips Res. Rep.* **31**, 167 (1958).
- ²⁴ M. Zouaghi, A. Coret, and J. O. Eymann, *Solid State Commun.* **7**, 311 (1969).
- ²⁵ S. V. Gastev, A. A. Kaplyanskii, and N. S. Sokolov, *Solid State Commun.* **42**, 389 (1982).
- ²⁶ N. Harukawa, S. Murakami, S. Tamon, S. Ijuin, A. Ohmori, and T. Abe, K. and Shigenari, *J. Lumin.* **87-89**, 1231 (2000).
- ²⁷ R. Garuthara and W. Siripala, *J. Lumin.* **121**, 173 (2006).
- ²⁸ S. Koirala, N. Naka, and K. Tanaka, *J. Lumin.* **134**, 524 (2013).
- ²⁹ S. Koirala, M. Takahata, Y. Hazama, N. Naka, and K. Tanaka, *J. Lumin.* **155**, 65 (2014).
- ³⁰ L. Frazer, K. B. Chang, R. D. Schaller, K. R. Poeppelmeier, and J. B. Ketterson, *J. Lumin.* **183**, 281 (2017).
- ³¹ M. Nolan, *Thin Solid Films* **516**, 8130 (2008).
- ³² D. O. Scanlon, B. J. Morgan, and G. W. Watson, *J. Chem. Phys.* **131**, 124703 (2009).
- ³³ B. Huang, *Solid State Commun.* **230**, 49 (2016).
- ³⁴ L. Y. Isseroff and E. A. Carter, *Chem. Mater.* **25**, 253 (2013).
- ³⁵ F. A. Kröger and H. J. Vink, *Solid State Phys.* **3**, 307 (1956)